

DOI: 10.1002/ ((please add manuscript number))

Article type: Full Paper

## **Efficient All-perovskite White Light-Emitting Diodes Made of *in-situ* Grown Perovskite-Mesoporous Silica Nanocomposites**

Meng Fan, Jinpeng Huang, Lyudmila Turyanska, Zhenfeng Bian, Liancheng Wang, Chunyang Xu, Nan Liu, Hongbo Li, Xiaoyu Zhang, Chengxi Zhang\* and Xuyong Yang\*

M. Fan, C. Xu, N. Liu, Dr. C. Zhang, Prof. X. Yang

Key Laboratory of Advanced Display and System Applications of Ministry of Education, Shanghai University, 149 Yanchang Road, Shanghai, 200072, China

E-mail: Andrew\_xiwa@shu.edu.cn; yangxy@shu.edu.cn

J. Huang, Prof. L. Wang

State Key Laboratory of High Performance Complex Manufacturing, College of Mechanical and Electrical Engineering, Central South University, Changsha, 410083, China

Dr. L. Turyanska

Faculty of Engineering, University of Nottingham, Nottingham, NG7 2RD, UK

Prof. Z. Bian

MOE Key Laboratory of Resource Chemistry and Shanghai Key Laboratory of Rare Earth Functional Materials, Shanghai Normal University, Shanghai, 200234, China.

Prof. H. Li

Experimental Center of Advanced Materials, School of Materials Science and Engineering, Beijing Institute of Technology, Beijing, 100081, China

Prof. X. Zhang

Key Laboratory of Automobile Materials Ministry of Education, College of Materials Science and Engineering, Jilin University, Changchun, 130012, China

**Abstract:** Metal halide perovskite quantum dots (QDs) have emerged as potential materials for high brightness, wide color gamut, and cost-effective backlight emission due to their high photoluminescence quantum yields (PLQYs), narrow emission linewidths, and tunable bandgaps. Herein, we prepare CsPbX<sub>3</sub>/SBA-15 nanocomposites with outstanding optical properties and high stability through an *in-situ* growth strategy using mesoporous silica particles. According to finite-difference time-domain (FDTD) simulations, the mesoporous structure provides a strong waveguide effect on perovskite QDs and the uniform dispersion suppresses reabsorption losses, improving the overall photoconversion efficiency of perovskite QDs. The as-fabricated perovskite monochromatic LED has a maximum luminous efficiency of 183 lm/W, which is the highest for monochromatic perovskite LEDs reported to date. A further benefit of this work is that the white devices, which combine the green and red perovskite nanocomposites with commercial blue LED, exhibit a high luminous efficiency of 116 lm/W and a wide color gamut (125% for NTSC and 94% for Rec. 2020) with coordinates of (0.33,0.31).

**Keywords:** Perovskite quantum dots; Reabsorption; Waveguide effect; Luminous efficacy; Light-emitting diodes.

## 1. Introduction

White light-emitting diodes (WLEDs) have been widely used commercially for general lighting and backlit displays due to their high power conversion efficiency and long lifespans.<sup>[1]</sup> Significant efforts are invested to improve the performance of white light devices in traditional display technologies.<sup>[2-5]</sup> However, the wide full-width-at-half-maximum (FWHM) of phosphors and the low efficiency of color converters limit the use of WLEDs in high luminous efficacy and wide color gamut displays.<sup>[6]</sup> Therefore, it is urgent to find more efficient and high-color saturation materials to reinforce the application prospects. Metal halide perovskites have attracted significant attention for applications in light-emitting diodes (LEDs),<sup>[7-10]</sup> solar cells,<sup>[11-14]</sup> photodetectors,<sup>[15]</sup> lasers, and mini/micro-LEDs,<sup>[16-18]</sup> due to their tunable optical properties,<sup>[19]</sup> near-unity ( $\sim 100\%$ ) photoluminescence quantum yield (PLQY), narrow emission linewidth and low materials cost.<sup>[20-24]</sup>

The fast crystallization kinetics and low formation energy of perovskites easily result in the formation of surface defects during the synthesis process and make them susceptible to decomposition under the influence of external conditions, such as the presence of moisture and oxygen,<sup>[1, 6]</sup> which affects the integrity of the crystal structure and decreases the luminous efficiency of the perovskite.<sup>[25]</sup> Moreover, part of the light emitted by the QDs is absorbed by the adjacent QDs and its conversion into thermal energy presents challenges for the performance stability of the LEDs.<sup>[2, 26]</sup> In particular, high concentrations of QDs increase the probability of agglomeration between QDs and thus aggravate reabsorption losses.<sup>[27]</sup> Perovskite-based white LED color converters

tend to have a low luminous efficacy of 20–80 lm/W,<sup>[7, 28]</sup> which limits their implementation in illumination and displays.<sup>[29, 30]</sup> In recent years, these issues have been greatly alleviated by encapsulation of QDs in polymers,<sup>[7]</sup> mesoporous alumina (Al<sub>2</sub>O<sub>3</sub>),<sup>[8]</sup> zeolite, metal-organic frameworks (MOFs),<sup>[2, 31]</sup> and mesoporous silica.<sup>[32-34]</sup> Although some promising encapsulation strategies have been proposed, there are still challenges in suppressing reabsorption losses to achieve high luminous efficacy and long operational stability.

In this work, we developed an *in-situ* growth strategy to synthesize highly luminescent CsPbX<sub>3</sub>/mesoporous silica (SBA-15) composites with outstanding optical properties and significantly improved stability. The structural characterization and a three-dimensional finite-difference time-domain (FDTD) modelling were performed to investigate the mechanism for the performance enhancement in these CsPbBr<sub>3</sub>/SBA-15 composites. We found that the ordered mesopore arrangement in the SBA-15 not only acts to avoid the agglomeration of perovskite QDs but also provides a strong optical waveguide effect, which effectively enhances the overall photoconversion efficiency of emitters due to the significantly reduced reabsorption loss. A monochromatic LED is achieved by integrating green-emitting perovskite composites onto a commercial blue LED chip, with a luminous efficacy of up to 183 lm/W, which is the highest reported to date for similar devices. Moreover, a wide color gamut (125% for NTSC) white all-perovskite LEDs with a luminous efficacy of 116 lm/W and color coordinates of (0.33,0.31) is achieved by silica gel encapsulation red and green perovskite composites.

## 2. Results and Discussion

The CsPbBr<sub>3</sub> QDs are synthesized using a modified hot-injection method<sup>[35]</sup> (see Experimental Section), and the mesoporous silica SBA-15 with a large specific surface area (550-650 m<sup>2</sup>/g), uniform two-dimensional hexagonal pore structure, high refractive index and structural stability is selected for coating the QDs.<sup>[25, 36, 37]</sup> Briefly, to *in-situ* synthesize perovskite QDs within the pores, PbO, phenacyl bromide and SBA-15 powder were mixed into 1-octadecene (ODE) solvent under a nitrogen atmosphere. The [PbBr<sub>6</sub>]<sup>4-</sup> was formed through a substitution reaction (see **Figure 1a**).<sup>[35]</sup> CsPbBr<sub>3</sub> QDs were formed upon injection of cesium oleate, which diffused into SBA-15 mesoporous structure. The crude CsPbBr<sub>3</sub>/SBA-15 composites were washed with isopropyl alcohol three times and dispersed in a hexane solution to remove perovskite QDs formed on the surface of the SBA-15. Moreover, halogen composition was modified by the anion exchange method to achieve CsPbX<sub>3</sub>/SBA-15 composites with different emission wavelengths. Finally, the composite powder was obtained by drying it under a vacuum at a temperature of 50 °C.

Transmission electron microscopic (TEM) images revealed that the orthorhombic CsPbBr<sub>3</sub> nanocrystals with an average size of  $\sim 9.4 \pm 0.3$  nm (**Figure S1**). The used SBA-15 molecular sieve has an ordered mesoporous structure with hexagonal pores of  $\sim 8.9$  nm (**Figure 1b** and **Figure S2**). The *in-situ* grown CsPbBr<sub>3</sub> in SBA-15 mesopores are found to be fully embedded in the SBA-15 mesopores with almost no un-encapsulated QDs presented on the surface (**Figure 1c**), which confirms the effectiveness of the washing procedure. The pore sizes of SBA-15 did not significantly

change after the formation of the composite, as expected for structurally stable and rigid SBA-15 (**Figure S3** and **Figure S4**).<sup>[37]</sup> The average size of the pore spacing is  $10.5 \pm 0.5$  nm, and the average size of the CsPbBr<sub>3</sub> QDs in SBA-15 matrix is 8.6 nm (**Figure S4c** and **Figure S4d**). The high-angle annular dark field-scanning TEM (HAADF-STEM) image and corresponding elemental mappings of CsPbBr<sub>3</sub>/SBA-15 confirm the presence of the CsPbBr<sub>3</sub> QDs throughout the SBA-15 matrix (**Figure 1d**).

To investigate the surface pore structure of CsPbBr<sub>3</sub>/SBA-15 composites, Brunauer–Emmett–Teller (BET) nitrogen adsorption-desorption isotherm was studied and revealed a typical type IV adsorption isotherm with sharp capillary condensation step and H1-type hysteresis loop at a higher relative pressure.<sup>[37, 38]</sup> With increasing relative pressure, monolayer adsorption and multilayer adsorption occur successively. When capillary condensation can occur under pressure, the adsorption isotherms become steeper, and finally the surface adsorption is observed. In the relative pressure range of 0.3-0.5, the adsorption capacity increases slowly, indicating the presence of mesoporous pores. At relative pressure  $P/P_0 = 0.62-0.95$ , the adsorption capacity increases rapidly, accompanied by an obvious H1 hysteresis loop, which is a typical phenomenon of mesopore capillary condensation, indicating that SBA-15 samples have regular pore size distribution and homogeneous mesoporous structure. Then, as the relative pressure continues to increase, the increase of adsorption capacity gradually slows down, indicating that the adsorption gradually reaches saturation (**Figure S5** and **Figure S6**). **Table S1** indicates the structural data of SBA-15 mesoporous particles based on the Barrett-Joyner-Halenda measurement. The specific surface area of SBA-

15 is about 627.99 m<sup>2</sup>/g and the pore width is around 8.84 nm. The specific surface area of CsPbBr<sub>3</sub>/SBA-15 decreases to 342.6 m<sup>2</sup>/g and pore volume also decreases from 1.27 cm<sup>3</sup>/g to 0.93 cm<sup>3</sup>/g, which indicates that the perovskites have been filled into the mesopore of SBA-15. Moreover, the pore diameter of CsPbBr<sub>3</sub>/SBA-15 kept a similar value (~ 8.9 nm), which is consistent with the TEM results, demonstrating the SBA-15 molecular sieve maintained a stable void structure after *in-situ* growth process.

Powder X-ray diffraction (XRD) patterns of the as-synthesized composites of CsPbBr<sub>3</sub>, SBA-15 and CsPbBr<sub>3</sub>/SBA-15 were recorded (**Figure 2a**). The control sample CsPbBr<sub>3</sub> QDs have diffraction peaks characteristic at 21.5° and 30.6° corresponding to (110) and (200) planes of orthorhombic CsPbBr<sub>3</sub>, respectively.<sup>[35]</sup> SBA-15 has a wide diffraction peak at 22.9°, which is consistent with the literature reports.<sup>[22]</sup> The spectra recorded for CsPbBr<sub>3</sub>/SBA-15 composites revealed diffraction peaks for both CsPbBr<sub>3</sub> and SBA-15, demonstrating that the crystal structure of the QDs synthesized *in situ* is not affected by the presence of the SBA-15 matrix. A slight shift of the composite CsPbBr<sub>3</sub> diffraction peak (0.15°) and a decrease in the intensity of the (200) peak is observed, which are due to the interaction between CsPbBr<sub>3</sub> and SBA-15 and the limitation of the growth within the mesopores.

The chemical compositions of both the CsPbBr<sub>3</sub> QDs and CsPbBr<sub>3</sub>/SBA-15 composites were studied by X-ray photoelectron spectroscopy (XPS) (**Figure S7**). The high-resolution XPS of the Br 3d (**Figure 2b**) revealed a small shift of peak positions (0.2 eV) indicative of the filling of Br-vacancy during *in-situ* growth. The Pb 4f spectra of CsPbBr<sub>3</sub>/SBA-15 reveals a blue shift of 0.8 eV in the peak position compared with

CsPbBr<sub>3</sub> QDs (**Figure 2c**), demonstrating that the SBA-15 has a coordination interaction with Pb<sup>2+</sup>. In addition, the two weak peaks of Pb 4f 142.08 eV and 137.18 eV are attributed to the defect sites of Pb<sup>0</sup> on the CsPbBr<sub>3</sub> QDs surface, whilst the vanishing Pb<sup>0</sup> signal in CsPbBr<sub>3</sub>/SBA-15 composite indicates inhibited the formation of Pb<sup>0</sup>. We envisage that the passivation of surface defects achieved with *in situ* growth strategy can reduce the nonradiative recombination rate of carriers.<sup>[39]</sup>

To further interrogate the interaction between CsPbBr<sub>3</sub> QDs and SBA-15, Fourier transforms infrared spectroscopy (FT-IR) measurements were performed (**Figure 2d**). A slight shift of the -OH peak of the CsPbBr<sub>3</sub>/SBA-15 composites was recorded compared to the SBA-15 alone, indicating the formation of H-bonds between the dangling functional groups presented in the mesopores and the halide anions in the perovskite crystals.<sup>[40]</sup> The absorption peak at 1396 cm<sup>-1</sup>, corresponding to the stretching vibration of -CH<sub>3</sub>, indicates the presence of lipophilic groups in SBA-15, which can adsorb ligands on the surface of perovskites, thereby preventing the shedding of ligands and reducing the formation of surface defects during the drying process.<sup>[41, 42]</sup>

The optical studies of composites produced with different ratios of perovskite to the SBA-15 (**Figure 3a**) revealed that the presence of the matrix increases the PL peak intensity of the perovskite QDs (centered at 520 nm), and the largest intensity was observed for CsPbBr<sub>3</sub>/SBA-15 with QD:SBA-5 ratio of 1:2 w/w. The PL peak of CsPbBr<sub>3</sub>/SBA-15 shown a small red shift (~1 nm) compared with CsPbBr<sub>3</sub> QDs, which due to the state of the material. The wavelength of CsPbBr<sub>3</sub> solution at 519 nm, while

CsPbBr<sub>3</sub>/SBA-15 were measured in the powder state. Therefore, the small red-shift can be attributed to the shorter distance between the QDs in the powder, resulting in enhanced interactions and a partial overlap of the wave functions. **Figure 3b** presents the luminescence and absorption spectra of the composites, emitting bright green and red light under 365nm UV irradiation (insets). For the CsPbBr<sub>3</sub> QDs (**Figure S8**), the PL peak is centered at  $\lambda_{PL} = 520$  nm with a full-width-at-half-maximum (FWHM) of 20 nm (**Table S2**), PLQY of 24.8% and an average PL decay lifetime ( $\tau_{ave}$ ) of 32.6 ns (**Figure 3c** and **Figure S9**). When CsPbBr<sub>3</sub> is grown in mesoporous SBA-15 molecular sieve, the PL peak and FWHM remain unchanged while the PLQY increases by 2.6 times, reaching the value of 63.96%, which we ascribe to the effect of the matrix, where in situ growth in the mesopores enables to achieve slower crystallization kinetics due to slower diffusion of cesium precursor into the pores.<sup>[30, 43]</sup>

Importantly, the CsPbBr<sub>3</sub> QDs are dispersed throughout the mesopores, hence preventing their agglomeration thus reducing the probability of photo-reabsorption, which is consistent with high PLQY.<sup>[44]</sup> The beneficial waveguide effect of SBA-15 is evident from the observed enhancement of optical properties.<sup>[36]</sup> We found that the PL lifetime of CsPbBr<sub>3</sub>/SBA-15 composite is prolonged to 104.97 ns compared to that of CsPbBr<sub>3</sub> QDs (32.6 ns) (**Table S3**), which we ascribe to the ordered arrangement of mesopores can decrease the ion diffusion rate to enhance the crystallinity and effectively passivate the surface defects of CsPbBr<sub>3</sub>. The short-lived ( $\tau_1$ ) and long-lived ( $\tau_2$ ) represent the non-radiative composite and radiative composite, respectively. The percentage of non-radiative recombination of CsPbBr<sub>3</sub>/SBA-15 (57%) lower than that

of CsPbBr<sub>3</sub> film (85%), corresponding to the PLQY increases from 24.84% to 63.96%. This indicates that the surface defects of the CsPbBr<sub>3</sub>/SBA-15 composite compared to the bare QDs are significantly decreases. The PL emission of the composite powder decreases by only 5% after being stored in the refrigerator at  $T = 5$  °C for up to six months (**Figure S10**), indicating that the mesoporous material can effectively prevent the intrusion of water oxygen and thus improve the material stability. Additionally, the mesoporous structure provides better dispersion for CsPbBr<sub>3</sub> and prevents the agglomeration phenomenon, thus reducing the probability of photo reabsorption.<sup>[44]</sup>

We successfully achieved *in-situ* control of halogen composition by anion exchange method and produced composites with tunable optical emissions in the range from 520 nm to 634 nm (**Figure S11**). The presence of SBA-15 matrix allows up to disperse the QDs, hence preventing the reabsorption of optical emission of the neighboring QDs, the random emission of light from tightly packed QDs will absorb each other and convert into the heat resulting in the reabsorption loss.<sup>[25]</sup> We propose that the optical waveguide effect of ordered mesopores structure can effectively inhibit the reabsorption between the QDs (**Figure 3d**).

FDTD simulations were performed to investigate the effect of structural parameters of SBA-15 on the reabsorption of inner CsPbBr<sub>3</sub> QDs. Based on the TEM structural analysis, the hexahedral arrangement was chosen for the model to simulate the optical transmission and absorption properties and to investigate the effects of parameters, such as pore width,  $w$ , and pore spacing,  $s$  (**Figure S12**). Herein, we defined the light extraction efficiency (LEE) as the transmittance ratio of the QD light of

CsPbBr<sub>3</sub>/SBA-15 to the QD light of CsPbBr<sub>3</sub>, and both materials are dispersed in a silica matrix. Three dipole sources with isotropic emission are considered as light sources for the QDs with wave vectors along the  $x$ ,  $y$  and  $z$  axes.<sup>[45]</sup> The relative refractive index (RRI) is the ratio of the refractive index of the mesoporous SBA-15 to that of the silicone resin, and the simulation results (**Figure 4a-b** and **Figure S13**) revealed that for  $RRI < 1$  the QD light is confined in the SBA-15 mesoporous structure owing to the high refractive index of silicone. In this case, the pores act as a waveguide structure, which inhibits the emission of light within the SBA-15, contributing to more reabsorption losses. For  $RRI = 1$ , the same refractive properties do not impact the transmission of light. Uniform dispersion is observed due to anisotropic emission of the CsPbBr<sub>3</sub> QDs. For  $RRI > 1$ , a clear mesoporous pattern can be seen on the electric field diagram; the ordered hole structure and internal scattering effect of SBA-15 provide the waveguide effect for the main subject, which bypasses the light emission to the adjacent CsPbBr<sub>3</sub> QDs, thus reducing the reabsorption losses and improving the optical conversion efficiency. These simulations demonstrate that with increasing RRI, the waveguide effect becomes more pronounced, enabling the transmission of QDs' emission through the composites.<sup>[6, 46]</sup>

To further investigate the effect of structural parameters on the waveguide effect, we consider  $RRI = 1.4$ . The energy of light decreases with increasing pore width from  $w = 6$  nm to 12 nm (**Figure 4c**), which is due to the increase in  $w$  will reduce the size of the main structure, resulting in a larger difference between the characteristic structure and the emission wavelength, thus weakening the waveguide effect. As the  $s$  increases,

the feature size required to confine the CsPbBr<sub>3</sub> QDs light increases, which enhances the waveguide effect (**Figure 4d-e**). In summary, the feature size ( $w, s$ ) of the mesopore structure is closely related to the waveguide effect. High RRI, small  $w$  and larger  $s$  are found to enhance the waveguide effect and reduce the reabsorption loss. However, from the perspective of *in-situ* growth, mesoporous materials with larger pore sizes are selected to achieve more reproducible control of the precursor diffusion and growth kinetics.

Two types of devices with CsPbBr<sub>3</sub> layer and with the composite CsPbBr<sub>3</sub>/SBA-15 were fabricated to investigate the benefits of the enhanced optical properties in CsPbBr<sub>3</sub>/SBA-15 composites on performance parameters of an LED. The emission of 460 nm blue chip (B) with an average luminous efficacy of 41.6 lm/W was used as the control device. Compared with CsPbBr<sub>3</sub> QDs LED, the composited CsPbBr<sub>3</sub>/SBA-15 LED exhibited a weaker absorption in the blue wavelength range and enhanced green light conversion (**Figure 5a**), demonstrating the mesoporous structure of SBA-15 can not only reduce the self-absorption of CsPbBr<sub>3</sub> QDs but also enhance the luminescence of CsPbBr<sub>3</sub>/SBA-15 due to the waveguide effect. We further optimized the mass ratio of perovskites to SBA-15 to enhance the luminous efficacy of monochromatic LED. Therein, GB and RGB refers to the addition of green emission material to the blue chip and the integration of red emission material and green emission material with the blue chip, respectively. Different proportions of the CsPbBr<sub>3</sub>/SBA-15 composites all exhibit enhanced luminous efficacy compared to CsPbBr<sub>3</sub> QDs (88.5 lm/W). The maximum luminous efficacy of monochromatic LEDs reaches 183 lm/W when the mass ratio of

CsPbBr<sub>3</sub> to SBA-15 is 1:2 w/w (**Figure 5b-c** and **Figure S14**), corresponding to a color gamut coordinate of (0.15,0.47) (**Figure S15**), which is the maximum luminous efficacy of monochromatic perovskite LEDs reported so far (**Table S4**). When the mass ratio of CsPbBr<sub>3</sub> to SBA-15 exceeds 1:2 w/w, causing a denser distribution of QDs in the pore, which results in a more serious reabsorption loss.

Encouraged by the enhanced luminous efficacy of CsPbBr<sub>3</sub>/SBA-15 monochromatic LED, we have further prepared a white LED using green CsPbBr<sub>3</sub>/SBA-15 and red CsPb(Br/I)<sub>3</sub>/SBA-15 composites with an optimized ratio of 1:2 w/w. With the addition of red composite, the luminous efficacy of the device is significantly reduced due to stronger absorption of blue light by red QDs, the red light having a smaller contribution to the luminosity function, hence lower luminous efficacy.<sup>[6]</sup> By optimizing the ratio of green to red composites, a white LED with a luminous efficiency of 116 lm/W is obtained (**Figure 5d**) with a color gamut coordinate of (0.33, 0.31) (**Figure S16**), which is higher than green/red perovskite QDs LED (87.8 lm/W) and green perovskite QDs/red phosphor LED (85 lm/W) (**Figure S17** and **Table S4**). The device displays a wide color gamut (125% of the National Television System Commission) with high luminous efficiency and high color rendering index (**Figure S18** and **Table S5**). Moreover, the emission spectra of the white LEDs are studied at different driving currents to verify the operating stability of the devices, and the results suggest that the color gamut coordinate of white LED slightly varied at currents from 10 mA to 70 mA (**Figure S19**), which is due to the blue luminescence intensity of blue chip is enhanced with the increase of current, but the absorption of blue light by red and

green composites has reached saturation, which leads to changes in color gamut coordinate white LED.<sup>[25]</sup>

### 3. Conclusion

We report a strategy to obtain CsPbBr<sub>3</sub>/SBA-15 composites with excellent optical properties and high stability by *in-situ* growth of CsPbBr<sub>3</sub> in mesoporous SBA-15. Analysis of the morphological structure and optical characteristics of the composites demonstrates that mesoporous SBA-15 can reduce the surface defects of CsPbBr<sub>3</sub>, resulting in a decrease in carrier non-radiative recombination rate, and a significant increase in luminescence lifetime. In addition, the FDTD method is adopted to simulate QD light extraction in CsPbBr<sub>3</sub>/SBA-15 with different structural parameters. The results indicate that the mesoporous structure of SBA-15 has a waveguide effect on QD light emission and significantly reduces reabsorption losses. We further verify that mesoporous materials lower reabsorption loss by comparing different mass ratios and QD contents through optimization experiments. With optimized parameters, green CsPbBr<sub>3</sub> LEDs achieved a maximum luminous efficacy of 183 lm/W reported for perovskite monochromatic LEDs so far. Furthermore, green and red composites were integrated to obtain all-perovskite white LEDs with a wide color gamut, and a luminous efficacy of 116 lm/W is achieved in the color gamut coordinates of (0.33, 0.31). The novel composite packaging strategy reported in this work presents a promising potential for optoelectronic applications.

#### 4. Experimental Section

*Materials:* Oleic acid (OA, 90%), 1-octadecene (ODE, technical grade, 90%) were purchased from Alfa Aesar. Lead(II) oxide (PbO, 99.999%) was purchased from Aladdin. Cesium carbonate ( $\text{Cs}_2\text{CO}_3$ , > 98%), oleylamine (OAm, 90%) were purchased from Acros. Phenacyl bromide ( $\text{C}_8\text{H}_7\text{BrO}$ , 97%) was purchased from Adamas. The mesoporous particles SBA-15 was purchased from Nanjing XFNANO Co. Ltd. Ethyl acetate, ethanol, hexane, and diethyl ether were purchased from Beijing Chemical Reagent Ltd., China. All chemicals were used as received without further purification.

*Preparation of Cs-oleate stock solution:* Cs-oleate was prepared following method reported in Ref.<sup>[47]</sup> 1.2 mmol of  $\text{Cs}_2\text{CO}_3$  was added to 18 ml of ODE and 2ml of OA in a three-necked flask, and degassed at 120 °C for 30 min under nitrogen. The reaction temperature was increased to 150 °C for 10 min to form a clear and transparent Cs-oleate solution.

*Synthesis of CsPbBr<sub>3</sub>/SBA-15 nanocomposites:* To synthesize the composite with QD to SBA-15 ratio of 1:2 w/w, 1 mmol of PbO, 3 mmol of phenacyl bromide and 1160 mg of SBA-15 were mixed with 5 ml of OA and 25 ml of ODE in a 100 ml three-neck flask and degassed under nitrogen for 30 min at 120°C. The temperature was then increased to 220°C and 2.5 ml of OAm was injected. The solution was heated for about 15 min and the color gradually changed from red to yellow. After that, the temperature was lowered to 180°C and 2.5 ml of Cs-oleate was injected swiftly. The solution was kept for 1 min and cooled to room temperature on an ice water bath. To obtain the final product, the compound powder was purified by washing twice with isopropanol and

dried under vacuum.

*Characterization methods:* The transmission electron microscopy (TEM) and scanning transmission electron microscopy (STEM) were carried out on a Tecnai G<sup>2</sup> (F30, FEI) transmission electron microscope operating at 300 kV. The energy-dispersive X-ray (EDX) spectrum was detected on the TEM to analyze the elemental composition. The X-ray diffraction (XRD) patterns were recorded on an X-ray diffractometer (D2 phaser, Bruker) with Cu K $\alpha$  radiation ranging from 10° to 60°. The absolute photoluminescence quantum yield (PLQY) and time-resolved fluorescence were measured on the Edinburgh FLS920 fluorescence spectrometer with a barium-sulfate-coated integrating sphere. The X-ray photoelectron spectra (XPS) were collected on a Kratos AXIS Ultra DLD X-ray photoelectron spectrometer. The Fourier transform infrared (FT-IR) spectra were recorded with a Nicolet Nexus 670 spectrometer. Specific surface areas were calculated using the BET (Brunauer–Emmett–Teller) method with N<sub>2</sub> adsorption–desorption isotherms recorded on a Micromeritics TriStar II 3020 specific surface and porosity analyzer.

*Device preparation:* The composite powder prepared by mixing specific proportions (the mass ratio of CsPbBr<sub>3</sub> to SBA-15 is 1:2 w/w, 60 mg) was added to silica gel (300 mg) in a certain mass ratio and the mixture was transferred to a planetary stirrer until it was uniformly dispersed. Finally, the obtained SBA slurry is dropped onto the blue LED chip (wavelength: 460 nm, luminous efficacy: 41.67 lm/W), thus completing the device preparation.

## **Supporting Information**

Supporting Information is available from the Wiley Online Library or from the author.

## **Acknowledgements**

The authors would like to thank the financial support from the National Key Research and Development Program of China (2022YFE0200200), National Natural Science Foundation of China (62174104, 61735004 and 52102182) and the Program of Shanghai Academic/Technology Research Leader (22XD1421200), China Postdoctoral Science Foundation (2020M680054, 2021T140440). LT acknowledges funding from the Engineering and Physical Sciences Research Council [grant number EP/P031684/1].

## **Author Contributions**

M.F. conducted LED device fabrication and performed most of characterizations and analysis. J.H. and L.W. discussed and performed the FDTD simulations. Z.B. analyzed BET data. C.X. and N.L. prepared the samples and analyzed the data. L.T., H.L. and X.Z. analyzed and discussed the experimental results. C.Z. and X.Y. designed and guided the project. All authors contributed to the manuscript.

## **Conflict of Interest**

The authors declare no competing financial interest.

Received: ((will be filled in by the editorial staff))

Revised: ((will be filled in by the editorial staff))

Published online: ((will be filled in by the editorial staff))

## References:

- [1] X. Wang, Z. Bao, Y. C. Chang, R. S. Liu, *ACS Energy Lett.* **2020**, *5*, 3374.
- [2] J. Ren, A. Meijerink, X. Zhou, J. Wu, G. Zhang, Y. Wang, *ACS Appl. Mater. Interfaces* **2022**, *14*, 3176.
- [3] S. Sadeghi, B. G. Kumar, R. Melikov, M. M. Aria, H. B. Jalali, S. Nizamoglu, *Optica* **2018**, *5*, 793.
- [4] T. Xuan, J. Huang, H. Liu, S. Lou, L. Cao, W. Gan, R. S. Liu, J. Wang, *Chem. Mater.* **2019**, *31*, 1042.
- [5] H. Wu, S. Wang, F. Cao, J. Zhou, Q. Wu, H. Wang, X. Li, L. Yin, X. Yang, *Chem. Mater.* **2019**, *31*, 1936.
- [6] J. S. Li, Y. Tang, Z. T. Li, J. X. Li, X. R. Ding, B. H. Yu, S. D. Yu, J. Z. Ou, H. C. Kuo, *ACS Nano* **2020**, *15*, 550.
- [7] C. Sun, Y. Zhang, C. Ruan, C. Yin, X. Wang, Y. Wang, W. W. Yu, *Adv. Mater.* **2016**, *28*, 10088.
- [8] B. Wang, C. Zhang, W. Zheng, Q. Zhang, Z. Bao, L. Kong, L. Li, *Chem. Mater.* **2019**, *32*, 308.
- [9] C. Zhang, S. Wang, X. Li, M. Yuan, L. Turyanska, X. Yang, *Adv. Funct. Mater.* **2020**, *30*, 1910582.
- [10] H. Wang, X. Gong, D. Zhao, Y. Zhao, S. Wang, J. Zhang, L. Kong, B. Wei, R. Quintero-Bermudez, O. Voznyy, Y. Shang, Z. Ning, Y. Yan, E. H. Sargent, X. Yang, *Joule* **2020**, *4*, 1977.
- [11] J. Y. Kim, J. W. Lee, H. S. Jung, H. Shin, N. G. Park, *Chem. Rev.* **2020**, *120*, 7867.

- [12] J. Liang, C. Wang, Y. Wang, Z. Xu, Z. Lu, Y. Ma, H. Zhu, Y. Hu, C. Xiao, X. Yi, *J. Am. Chem. Soc.* **2016**, 138, 15829.
- [13] H. S. Jung, G. S. Han, N. G. Park, M. J. Ko, *Joule* **2019**, 3, 1850.
- [14] J. Wei, Q. Wang, J. Huo, F. Gao, Z. Gan, Q. Zhao, H. Li, *Adv. Energy Mater.* **2021**, 11, 2002326.
- [15] H. Jing, R. Peng, R. M. Ma, J. He, Y. Zhou, Z. Yang, C. Y. Li, Y. Liu, X. Guo, Y. Zhu, D. Wang, J. Su, C. Sun, W. Bao, M. Wang, *Nano Lett.* **2020**, 20, 7144.
- [16] L. Lei, Q. Dong, K. Gundogdu, F. So, *Adv. Funct. Mater.* **2021**, 31, 2010144.
- [17] Y. Liu, F. Li, L. Qiu, K. Yang, Q. Li, X. Zheng, H. Hu, T. Guo, C. Wu, T. W. Kim, *ACS Nano* **2019**, 13, 2042.
- [18] C. Zhang, J. Chen, L. Turyanska, J. Wang, W. Wang, L. Wang, L. Kong, K. Wu, J. Yao, H. Yao, Z. Yang, W. Li, Y. Bekenstein, Y. Wang, G. Jia, X. Yang, *Adv. Funct. Mater.* **2022**, 2211466.
- [19] Z. Ma, X. Li, C. Zhang, L. Turyanska, S. Lin, X. Xi, J. Li, T. Hu, J. Wang, A. Patane, L. Zhao, *ACS Appl. Nano Mater.* **2021**, 4, 8383.
- [20] C. Y. Kang, C. H. Lin, C. H. Lin, T. Y. Li, S. W. H. Chen, C. L. Tsai, C. W. Sher, T. Z. Wu, P. T. Lee, X. Xu, M. Zhang, C. H. Ho, J. H. He, H. C. Kuo, *Adv. Sci.* **2019**, 6, 1902230.
- [21] C. H. Lin, C. Y. Kang, A. Verma, T. Wu, Y. M. Pai, T. Y. Chen, C. L. Tsai, Y. Z. Yang, S. K. Sharma, C. W. Sher, Z. Chen, P. T. Lee, S. R. Chung, H. C. Kuo, *Nanomaterials* **2019**, 9, 1314.
- [22] Q. Zhang, W. Zheng, Q. Wan, M. Liu, X. Feng, L. Kong, L. Li, *Adv. Optical Mater.*

2021, 9, 2002130.

- [23] Y. Cai, Y. Li, L. Wang, R. J. Xie, *Adv. Optical Mater.* **2019**, 7, 1901075.
- [24] Z. Liu, Y. Zhang, Y. Fan, Z. Chen, Z. Tang, J. Zhao, Y. lv, J. Lin, X. Guo, J. Zhang, X. Liu, *ACS Appl. Mater. Interfaces* **2018**, 10, 13053.
- [25] J. Li, Y. Tang, Z. Li, X. Ding, B. Yu, L. Lin, *ACS Appl. Mater. Interfaces* **2019**, 11, 18808.
- [26] B. Xie, H. Liu, R. Hu, C. Wang, J. Hao, K. Wang, X. Luo, *Adv. Funct. Mater.* **2018**, 28, 1801407.
- [27] I. Coropceanu, M. G. Bawendi, *Nano Lett.* **2014**, 14, 4097.
- [28] W. Yang, F. Gao, Y. Qiu, W. Liu, H. Xu, L. Yang, Y. Liu, *Adv. Optical Mater.* **2019**, 7, 1900546.
- [29] K. T. Shimizu, M. Böhmer, D. Estrada, S. Gangwal, S. Grabowski, H. Bechtel, E. Kang, K. J. Vampola, D. Chamberlin, O. B. Shchekin, J. Bhardwaj, *Photonics Research* **2017**, 5, A1.
- [30] S. Yu, Y. Tang, Z. Li, K. Chen, X. Ding, B. Yu, *Photonics Research* **2018**, 6, 90.
- [31] Y. Zhang, L. Han, B. Li, Y. Xu, *Chem. Eng. J.* **2022**, 437, 135290.
- [32] C. F. Lai, Y. C. Chang, Y. S. Huang, *Nanomaterials* **2022**, 12, 1554.
- [33] S. Pathak, N. Sakai, F. W. R. Rivarola, S. D. Stranks, J. Liu, G. E. Eperon, C. Ducati, K. Wojciechowski, J. T. Griffiths, A. A. Haghighirad, A. Pellaroque, R. H. Friend, H. J. Snaith, *Chem. Mater.* **2015**, 27, 8066.
- [34] E. R. Dohner, A. Jaffe, L. R. Bradshaw, H. I. Karunadasa, *J. Am. Chem. Soc.* **2014**, 136, 13154.

- [35] S. Bera, R. K. Behera, N. Pradhan, *J. Am. Chem. Soc.* **2020**, 142, 20865.
- [36] M. Kalhor, S. M. Sajjadi, A. Dadras, *RSC Adv.* **2020**, 10, 27439.
- [37] J. Y. Sun, F. T. Rabouw, X. F. Yang, X. Y. Huang, X. P. Jing, S. Ye, Q. Y. Zhang, *Adv. Funct. Mater.* **2017**, 27, 1704371.
- [38] H. Xu, H. Yang, G. Xu, Y. Yang, *MATEC Web of Conferences* **2016**, 67, 01006.
- [39] H. H. Zhang, Z. C. Zhou, Y. J. Dong, L. Zhang, H. Y. Chen, D. B. Kuang, *Sol. RRL* **2021**, 5, 2100559.
- [40] P. Wang, B. Wang, Y. Liu, L. Li, H. Zhao, Y. Chen, J. Li, S. Liu, K. Zhao, *Angew. Chem.* **2020**, 132, 23300.
- [41] Z. Li, C. Song, J. Li, G. Liang, L. Rao, S. Yu, X. Ding, Y. Tang, B. Yu, J. Ou, U. Lemmer, G. Gomard, *Adv. Mater. Technol.* **2020**, 5, 1900941.
- [42] J. S. Ghomi, A. Bakhtiari, *ChemistrySelect* **2018**, 3, 12704.
- [43] W. Wang, R. Guo, X. Xiong, H. Liu, W. Chen, S. Hu, E. Amador, B. Chen, X. Zhang, L. Wang, *Mater. Today Phys.* **2021**, 18, 100374.
- [44] V. Malgras, J. Henzie, T. Takei, Y. Yamauchi, *Angew. Chem.* **2018**, 130, 9019.
- [45] Z. T. Li, I. Member, J. X. Li, J. S. Li, Z. H. Deng, Y. H. Deng, Y. Tang, *IEEE J Quantum Electron* **2020**, 56, 1.
- [46] J. S. Li, Y. Tang, Z. T. Li, X. R. Ding, L. S. Rao, B. H. Yu, *IEEE Trans Electron Devices* **2018**, 65, 2877.
- [47] L. Protesescu, S. Yakunin, M. I. Bodnarchuk, F. Krieg, R. Caputo, C. H. Hendon, R. X. Yang, A. Walsh, M. V. Kovalenko, *Nano Lett.* **2015**, 15, 3692.

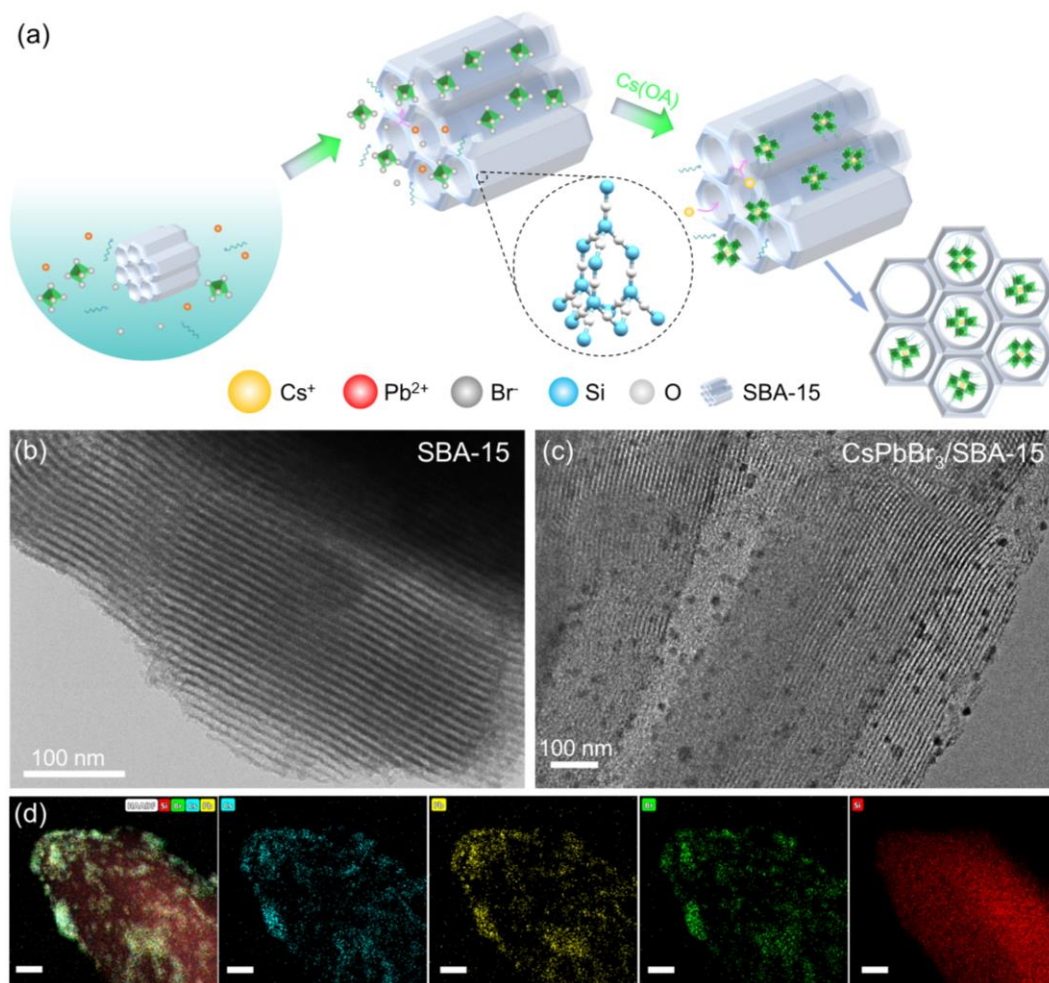


**Figure 1.** (a) Schematic illustration of the *in-situ* synthesis of CsPbBr<sub>3</sub>/SBA-15 composites. (b) TEM image of SBA-15. (c) TEM image of CsPbBr<sub>3</sub>/SBA-15. (d) HAADF STEM image and the corresponding elemental mappings of Cs, Pb, Br and Si elements. Scale bars: 100 nm.

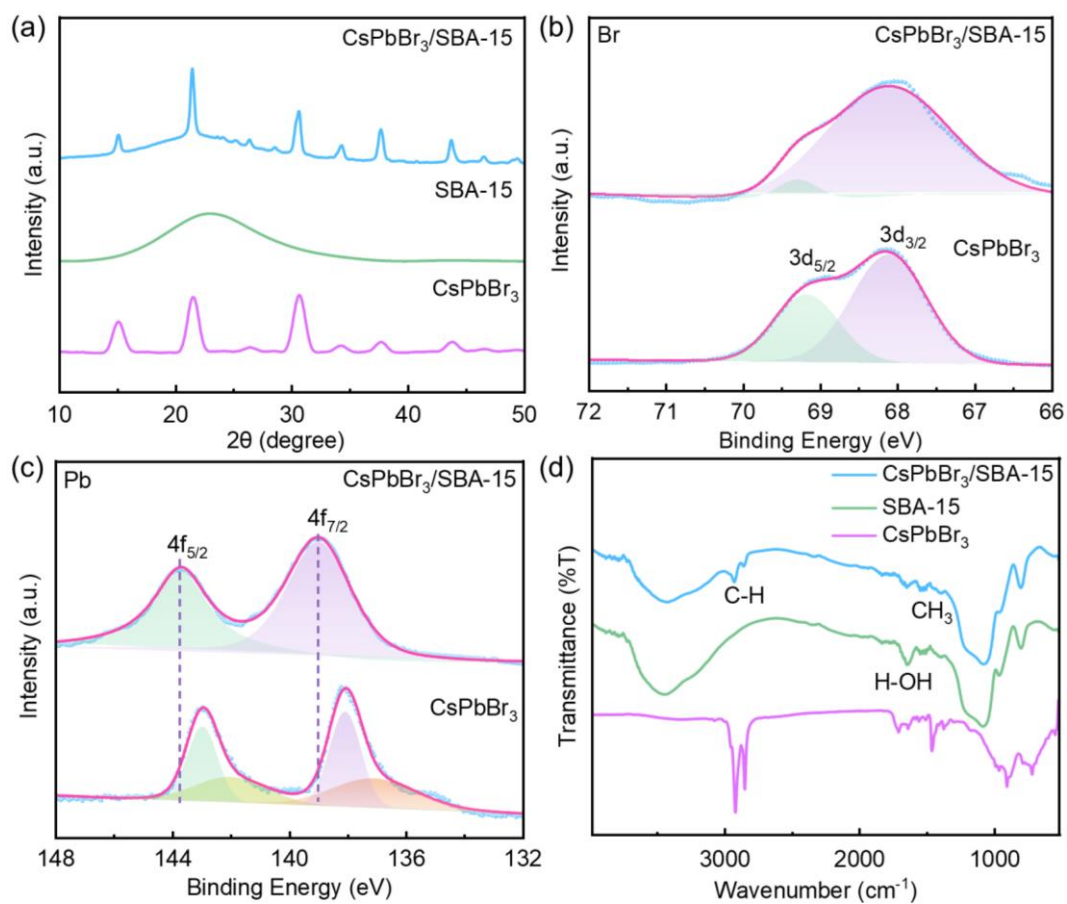


**Figure 2.** Characterization of CsPbBr<sub>3</sub>/SBA-15 composites. (a) X-ray diffraction patterns of CsPbBr<sub>3</sub>, SBA-15 and CsPbBr<sub>3</sub>/SBA-15. (b) High-resolution X-ray photoelectron spectra (XPS) of Br 3d. (c) High-resolution XPS of Pb 4f. (d) FT-IR spectra of CsPbBr<sub>3</sub>, SBA-15 and CsPbBr<sub>3</sub>/SBA-15 composites, respectively.

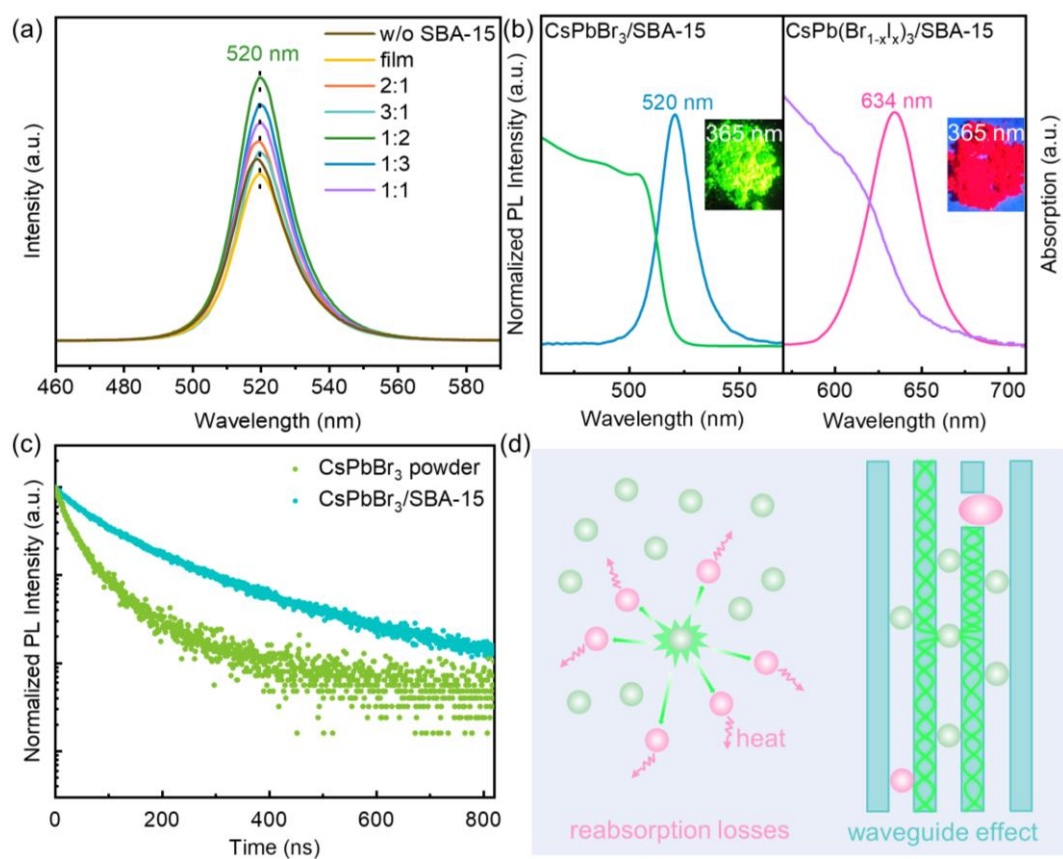


**Figure 3.** (a) Photoluminescence of composites with different mass ratios and naked QDs (b) Photoluminescence emission and absorption spectra and photograph (insets) of the composites with various halide composition under UV excitation at 365 nm. (c) Time-resolved PL decays of CsPbBr<sub>3</sub> powder and CsPbBr<sub>3</sub>/SBA-15 composites. (d) Schematic illustration of the reabsorption losses and waveguide effect.

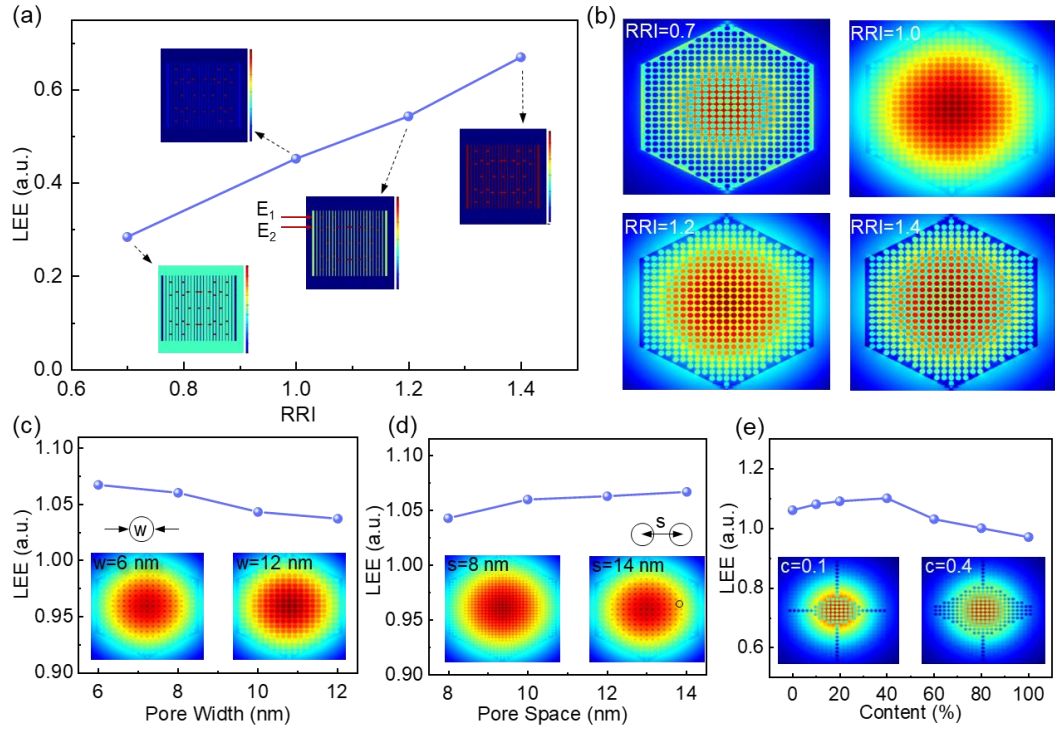


**Figure 4.** FDTD simulation of CsPbBr<sub>3</sub>/SBA-15 composites. (a) LEE of CsPbBr<sub>3</sub>/SBA-15 with different RRIs. The insets show the different refractive indices of CsPbBr<sub>3</sub>/SBA-15 and the observed directions of electric field monitors E<sub>1</sub> and E<sub>2</sub>. (b) The electric field distribution of CsPbBr<sub>3</sub>/SBA-15 with different RRI values as observed by monitor E<sub>1</sub>. (c-e) The LEE of LHP QDs light in CsPbBr<sub>3</sub>/SBA-15 with different pore widths *w*, pore spacings *s* and QDs contents.

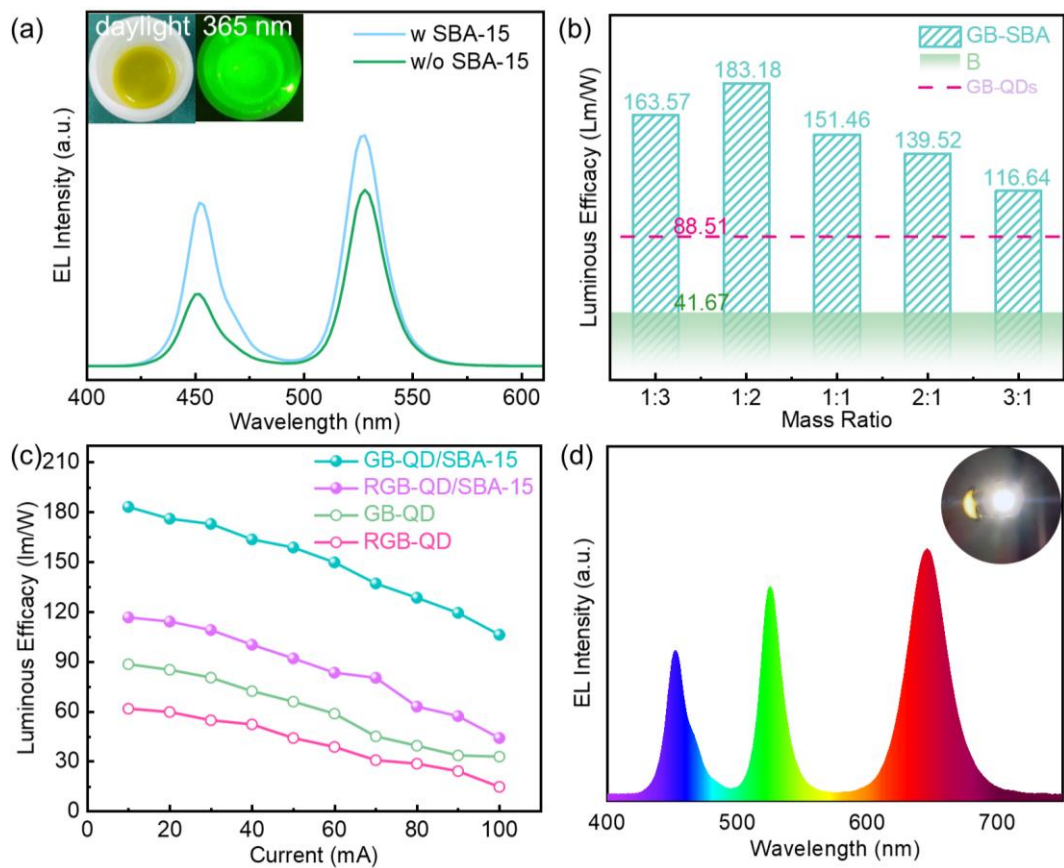


**Figure 5.** (a) Emission spectra of perovskite monochromatic LEDs fabricated according to green composites and material object figure (insets). (b) Luminous efficacy of CsPbBr<sub>3</sub>/SBA-15 LEDs with different mass ratios. (d) Emission spectrum of white LED with integrated green and red composites and physical photograph (inset).